AIAA JOURNAL
Vol. 51, No. 3, March 2013

Geometric Optimization of a Cylindrical Plasma Adaptive Optics Lens

Brian W. Neiswander,* Eric Matlis,† and Thomas C. Corke‡
University of Notre Dame, Notre Dame, Indiana 46556

DOI: 10.2514/1.J052029

Plasma is a dynamic optical medium with potential applications in the field of aero-optics for wavefront control. The objective is to develop "plasma adaptive optic" devices which rely upon the relationship between plasma electron density and index of refraction. The advantages of plasma adaptive optic devices are that they have no moving parts and can have temporal responses two orders of magnitude higher than the fastest deformable mirror. Therefore, plasma adaptive optic devices have the potential to be more robust, less subject to fatigue, and faster than conventional technology. Experimental results and a theoretical model are presented which investigate the spatial distribution of the plasma inside a cylindrical plasma adaptive optic lens. The experiment reveals two distinct plasma formation regimes that occur depending on the lens geometry. The theoretical model is used to help identify the geometric parameters required to produce each plasma regime. The excellent agreement between the experiment and theory provides a scaling relation for the cylindrical plasma adaptive optic lens. This scaling relation is necessary for the future design of an array of plasma adaptive optics to provide spatial wavefront corrections for aero-optic applications.

Nomenclature

a	=	distance between **P** and $\mathbf{P}_0$
D	=	electrode diameter
d	=	electrode-gap distance
$\mathrm{d}q$	=	differential charge of point source
$\mathrm{d}V$	=	differential voltage of point source
$\mathrm{d}\theta$	=	differential change in azimuthal angle around electrode
E	=	complete elliptic integral of the second kind
E	=	magnitude of electric field
$\mathbf{E}_{\mathrm{ring}}$	=	electric field vector of a charged ring
E_z	=	axial component of electric field
$E_{z,\mathrm{ring}}$	=	axial component of electric field of a charged ring
E_θ	=	azimuthal component of electric field
$E_{\theta,\mathrm{ring}}$	=	azimuthal component of electric field of a charged ring
E_ρ	=	radial component of electric field
$E_{\rho,\mathrm{ring}}$	=	radial component of electric field of a charged ring
$\hat{e}_z$	=	unit vector in z direction
$\hat{e}_\theta$	=	unit vector in θ direction
$\hat{e}_\rho$	=	unit vector in ρ direction
$\hat{i}$	=	unit vector in x direction
$\hat{j}$	=	unit vector in y direction
K	=	complete elliptic integral of the first kind
$\hat{k}$	=	unit vector in z direction
P	=	vector to an arbitrary point in the yz plane
$\mathbf{P}_0$	=	vector to a point on electrode
q	=	charge
R	=	electrode radius
V	=	voltage potential
V_{ring}	=	voltage potential of a charged ring
z	=	distance to **P** along the z axis
α	=	geometry parameter
β	=	geometry parameter
γ	=	geometry parameter
ϵ_0	=	vacuum permittivity constant
θ	=	angle in the xy plane
ρ	=	distance to **P** along the x axis
$\rho_{\mathrm{inflection}}$	=	radius to the inflection point
ρ_{max}	=	radius to the maximum value
ρ^*_{max}	=	radius to the maximum value normalized by the total radius
ρ^{**}_{max}	=	radius to the maximum value normalized by the inflection radius

Presented as Paper 2012-0625 at the 50th Aerospace Sciences Meeting, Nashville, TN, 9–12 January 2012; received 12 April 2012; revision received 17 July 2012; accepted for publication 23 July 2012; published online 23 November 2012.

*Ph.D. Candidate, Aerospace and Mechanical Engineering; bneiswan@nd.edu. Student member AIAA.

†Assistant Research Professor, Aerospace and Mechanical Engineering; ematlis@nd.edu. Member AIAA.

‡Clark Chair Professor, Aerospace and Mechanical Engineering; tcorke@nd.edu. Fellow AIAA.

I. Introduction

DIRECTED energy and laser-communications technology in aerospace applications rely on the use of adaptive optics (AO) systems for sufficient energy delivery and data transfer. As a laser beam passes through shear layers and turbulence in the wake of a moving aircraft, density gradients can cause distortions, or aberrations, in the beam wavefronts. Aberrations are characterized in terms of optical path difference (OPD), which is the physical length to which the wavefront is distorted. Wavefront OPDs significantly reduce the intensity of a beam as it propagates into the far field [1]. When insufficient energy reaches the far field, OPDs can prevent a target's destruction and inhibit data transfer. Past in-flight measurements of root-mean-square OPD have fallen in the range from 0 to 0.25 μm [2].

AO systems utilize closed-loop control schemes to correct for OPDs and restore planar wavefronts. An AO system typically comprises a wavefront sensor to measure the OPD, a controller to process and prescribe corrections, and an active wavefront control device to correct for aberrations. An example of an AO system is shown in Fig. 1. The control device is typically a deformable mirror that is a segmented or continuous reflective surface that spatially distorts itself to reflect back planar wavefronts. Deformable mirrors are electromechanical devices that have some inertial limitations. Correction rates typically range from hundreds of hertz to a few kilohertz. Mechanical deformable mirrors are generally delicate and eventually fail because of material fatigue. Therefore, there is a desire to develop more robust wavefront control devices that also might have improved frequency response.

Under appropriate conditions, the index of refraction of a plasma varies linearly with its electron density [3]. Because the plasma

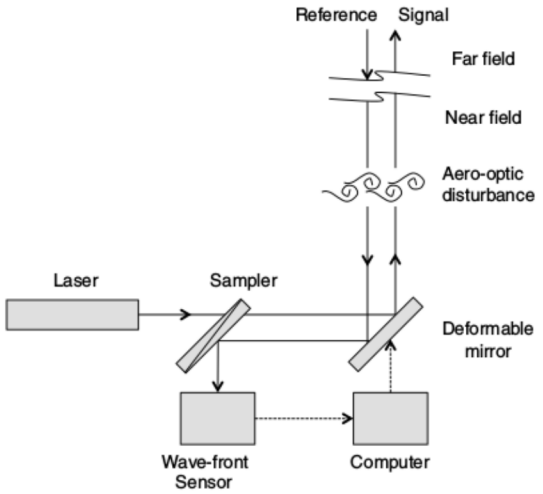

Fig. 1 A schematic of a conventional AO system that uses a deformable mirror.

electron density can be varied through its applied electric field, this approach can provide a method for dynamically controlling the index of refraction. If the plasma is confined within a volume, it is possible to effectively create a "plasma lens" with a variable index of refraction. The frequency response of such a plasma lens is only limited by the recombination time of electrons and ions and therefore should be in the range of hundreds of kilohertz [4]. This would easily exceed, by two orders of magnitude, the fastest deformable mirrors now available.

II. Preliminary Experiments

Proof of concept work by the authors used interferometry to characterize the spatial OPD profile from a cylindrical plasma adaptive optics (PAO) lens [5]. These experiments used a PAO lens 15.2 cm in length and 1.9 cm in diameter. A schematic of the lens is shown in Fig. 2. The lens provided a long length of plasma for the laser to pass through and achieved OPD values greater than 1 μm [5]. However, because of the large separation of the electrodes, the PAO lens required a relatively larger amount of power to generate the plasma.

One motivation for making smaller PAO lenses is that it would reduce the operation power consumption, which would be important with array configurations like the one conceptualized in Fig. 3. In this concept, the optical wavefront control system would consist of a two-dimensional array of PAOs that cover a conventional rigid mirror. The voltage potential to the individual plasma lenses would be individually controlled so that a large-scale spatially coherent wavefront distortion could be produced. A similar approach is used in plasma display panels of plasma televisions, although in that case the light emission property of the plasma is utilized [4, 6], rather than the wavefront distortion property.

Initial experiments to miniaturize the cylindrical PAO lens revealed an interesting plasma behavior. At very small electrode-gap distances, the plasma formed along the inside wall of the lens, whereas at large gap distances, the plasma formed in the center of the

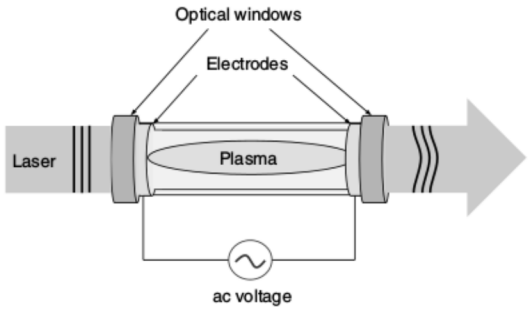

Fig. 2 Schematic of a cylindrical PAO lens.

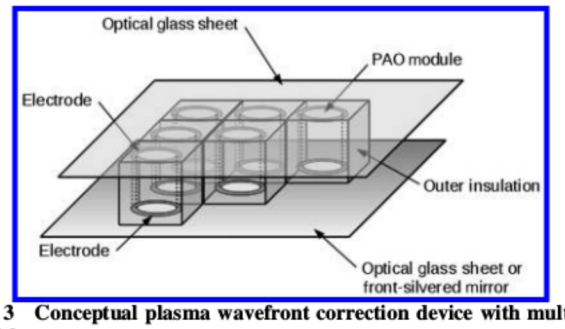

Fig. 3 Conceptual plasma wavefront correction device with multiple PAO lenses.

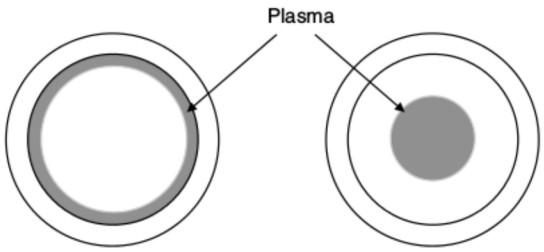

a) Small *d/D* **b) Large *d/D***

Fig. 4 Plasma regimes observed inside the PAO lens: a) wall-plasma and b) center-plasma.

cylindrical lens. The two plasma formation regimes are depicted in Fig. 4. From these experiments, the physical quantity that was determined to be the deciding factor in selecting the plasma formation regime was the ratio of the distance between the electrodes, d, and the inside diameter of the cylinder lens, D, namely, d/D. The underlying physics behind the selection process was unknown, but critical to optimizing the PAO performance.

III. Objective

The overall object of this work was to optimize the geometry of a PAO lens. For this, the emphasis was on cylindrical geometries like that shown in Fig. 2. In this, a specific objective was to identify the geometric dependencies and underlying physics of the PAO lens that leads to the two plasma regimes brought out in the preliminary experiments. A theoretical model for the behavior that is validated by the experiments was also sought.

IV. Experimental Setup

A. Adjustable Plasma Adaptive Optics Lens

The experiments used a cylindrical PAO lens arrangement with an adjustable electrode-gap distance. A schematic drawing and photograph of the setup is shown in Fig. 5. It featured a hollow borosilicate tube with a 9.0 mm outer diameter and a 1.0 mm thick wall. The tube was 100 mm long. It passed through three acrylic blocks. The two end blocks were fixed to the base. They had optical windows that allowed optical access to the interior of the hollow tube. The center block was movable. Its position was driven by a lead screw that passed through it. Turning the lead screw caused the middle block to translate along the tube.

Two brass electrode collars were positioned on the outside of the borosilicate tube. The collars were 6.35 mm long in the tube axial direction, with a 10 mm outer diameter and a 0.9 mm thick wall. The right electrode collar was fixed to the rightmost acrylic block. The left electrode collar was attached to the sliding acrylic block. Rotating the lead screw therefore allowed for accurate adjustment of the gap distance between the two electrodes. The gap distance was measured with Cen-Tech digital calipers to an accuracy of 0.01 mm.

B. Plasma Generation

For the experiments, the gas inside the PAO lens was air at different static pressures. As discussed in our previous work [5], other gases

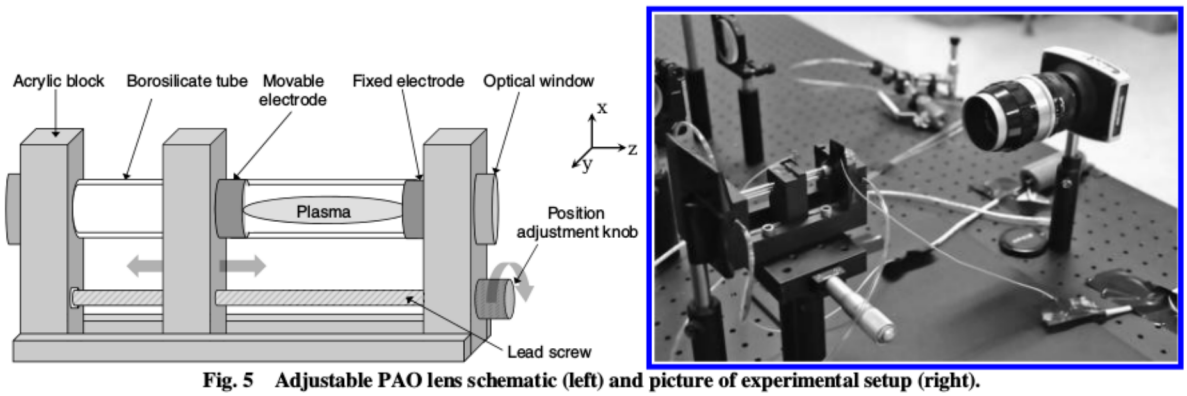

Fig. 5 Adjustable PAO lens schematic (left) and picture of experimental setup (right).

are preferable for optimum PAO designs. However, the geometric scaling issues examined in this paper are independent of the gas used because the proposed model neglects the gas and plasma inside the PAO lens.

The pressure inside the adjustable PAO lens was lowered using a JB Platinum DV-285N vacuum pump that was connected to a port in one of the acrylic end blocks. The pressure was measured with a Heise H51011 absolute pressure gauge. A large ac voltage potential was applied across the two electrodes to generate a plasma inside the hollow tube. The ac signal was a 14 kHz sine wave that was produced by an Agilent 33220A function generator. Two Crown XTi4000 amplifiers and two Corona Magnetics transformers were used to boost the voltage amplitude of the function generator output. The high-voltage signal was measured with a LeCroy PHV4-1903 high-voltage probe. Current was measured with a Pearson 2100 current monitor. The voltage and current measurements were acquired using a LeCroy WaveRunner LT264 oscilloscope and downloaded to a computer using a transmission control protocol connection.

C. Image Acquisitions

Images of the plasma inside the adjustable PAO lens were recorded with a Spot Idea digital camera having a 5 megapixel resolution and a 12 bit color depth. The camera lens was a Micro-Nikkor 55 mm lens that was set at an $f/8$ aperture. The image exposure time was 2.3 s. The camera was positioned to view through the optical windows and into the PAO lens.

V. Experimental Results

Twelve electrode-gap distances were tested for the PAO lens arrangement. They ranged from 2.7 mm to 12.6 mm. Each gap distance represents a unique d/D value. The pressure inside the PAO lens was held constant at 25.8 torr. The peak-to-peak voltage potential that was used to sustain a stable plasma inside the adjustable PAO lens was measured for each gap distance. The method used to define a stable PAO plasma was presented by Neiswander [5]. The gap distances, d/D ratios, and voltage potentials used in the experiment are listed in Table 1.

Table 1 Electrode-gap distances, d/D ratios, and applied voltages used in the experiment

d, mm	d/D	Voltage, kV
2.7	0.3	1.8
3.6	0.4	2.3
4.5	0.5	2.2
5.4	0.6	3.0
6.3	0.7	3.2
7.2	0.8	3.5
8.1	0.9	3.5
9.0	1.0	3.5
9.9	1.1	3.5
10.8	1.2	3.5
11.25	1.25	3.5
12.6	1.4	3.5

For each gap distance, an image of the plasma luminescence inside the PAO lens was acquired. These images are shown in Fig. 6. The images were postprocessed to generate an azimuthally averaged radial profile of the plasma for each gap distance. These radial profiles are shown in Fig. 7. The gray scales in the images vary from image to image to better emphasize the change in spatial structure of the plasma luminescence.

The plasma luminescence profiles in Fig. 7 clearly show the wall-plasma and center-plasma regimes. At the smallest gap distance of $d/D = 0.3$, the plasma layer was very thin and directly on the surface of the inside cylinder wall of the PAO lens. As the gap distance increased up to $d/D = 0.5$, the plasma layer thickened but remained attached to the inside cylinder wall. As the gap distance increased above $d/D = 0.5$, the plasma remained attached to the inside cylinder wall, but the radial location of the maximum luminescence began to move toward the center of the cylindrical PAO lens. At $d/D = 1.25$, the plasma fully coalesced in the center of the cylindrical PAO lens. At larger values of d/D, the plasma remained in the center cylindrical PAO lens. Based on these results, the critical d/D value that separates the two plasma distribution regimes in the cylindrical PAO lens is $d/D = 1.25$.

VI. Theory

To better understand the wall-plasma and center-plasma regimes observed in the experiment, an electrostatic model for the cylindrical PAO lens was derived. The assumptions for the analytical model are 1) steady-state, 2) axisymmetric, 3) no dielectric present, 4) no plasma present, and 5) infinitely thin electrodes.

A. Voltage Potential of a Charged Ring

The theoretical formulation begins by considering a charged ring of radius R in the xy plane, as illustrated in Fig. 8. The vector location of a point, $\mathbf{P}_0$, on the radius of the charged ring is

$$\mathbf{P}_0 = R\cos\theta\hat{i} + R\sin\theta\hat{j} + 0\hat{k} \tag{1}$$

The vector location of an arbitrary point, $\mathbf{P}$, is

$$\mathbf{P} = \rho\hat{i} + 0\hat{j} + z\hat{k} \tag{2}$$

The distance a between $\mathbf{P}_0$ and $\mathbf{P}$ is therefore

$$a = (\rho^2 + R^2 + z^2 - 2\rho R\cos\theta)^{1/2} \tag{3}$$

The differential voltage potential at $\mathbf{P}$ due to the charge at $\mathbf{P}_0$ is

$$\mathrm{d}V = \frac{1}{4\pi\epsilon_0}\frac{dq}{a} \tag{4}$$

where $\epsilon_0 = 8.85418 \times 10^{-12}$ Fm^{-1} is the vacuum permittivity and the differential charge is

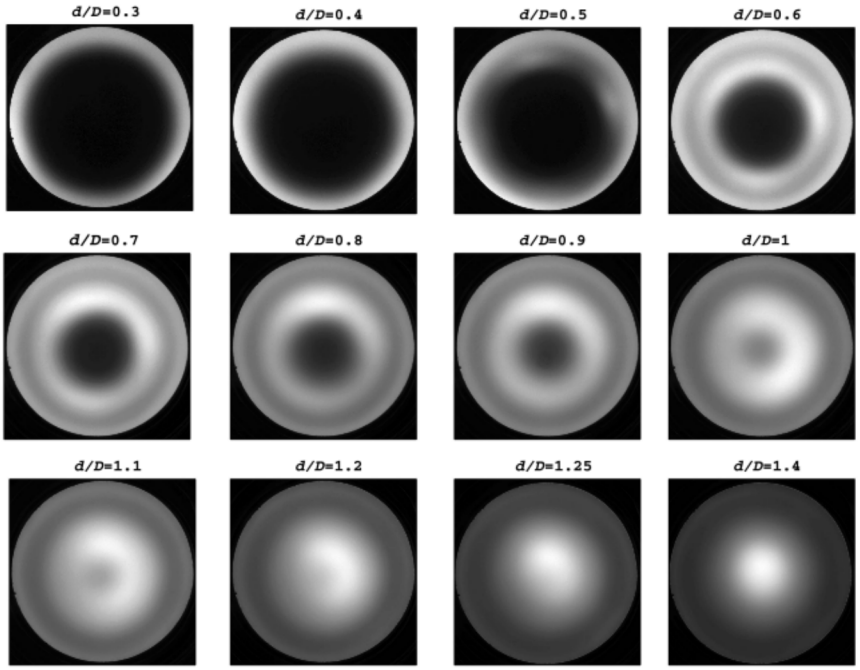

Fig. 6 Experimental images of the plasma luminescence for different d/D ratios.

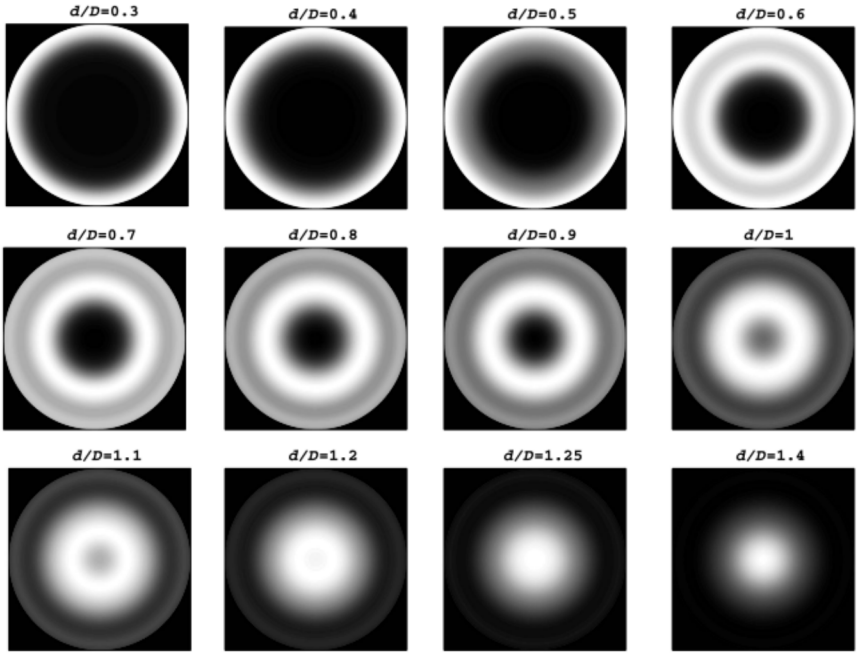

Fig. 7 Azimuthally averaged profiles of the plasma luminescence for different d/D ratios.

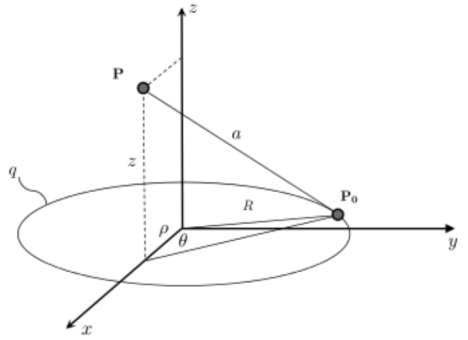

Fig. 8 Illustration of a charged ring in the xy plane.

$$dq = \frac{q}{2\pi R} R d\theta \tag{5}$$

An expression for the voltage potential at **P** induced by a ring of charge lying in the xy plane is found from integrating the differential voltage potential in Eq. (4) over the interval $\theta = [0, 2\pi]$. Observing the symmetry in the integral, this becomes

$$V = \frac{q}{4\pi^2 \epsilon_0 \rho} \int_0^{\pi} \frac{d\theta}{(\rho^2 + z^2 + R^2 - 2\rho R \cos\theta)^{1/2}} \tag{6}$$

This can be rewritten as

$$V = \frac{q}{4\pi^2 \epsilon_0 \rho} \left(\frac{1}{2\rho R}\right)^{1/2} \int_0^{\pi} \frac{d\theta}{(b - \cos\theta)^{1/2}} \tag{7}$$

where

$$b = \frac{\rho^2 + R^2 + z^2}{2\rho R} \tag{8}$$

Equation 7 is an elliptic integral with the solution

$$V_{\text{ring}} = \frac{q}{2\pi^2\epsilon_0}\frac{1}{\alpha}\mathrm{K}\left(\frac{4R\rho}{\alpha}\right) \tag{9}$$

where K in Eq. (9) is the complete elliptic integral of the first kind [7,8]. The parameter α is

$$\alpha = (\rho + R)^2 + z^2 \tag{10}$$

Equation 9 gives the voltage potential at any point in the xy plane due to a charged ring of radius R located in the xy plane and centered at the origin.

B. Electric Field of a Charged Ring

The electric field is the negative gradient of the potential. For a single charged ring, the electric field is

$$\mathbf{E}_{\text{ring}} = -\nabla V_{\text{ring}} = -\frac{\partial V_{\text{ring}}}{\partial \rho}\hat{e}_\rho - \frac{1}{\rho}\frac{\partial V_{\text{ring}}}{\partial \theta}\hat{e}_\theta - \frac{\partial V_{\text{ring}}}{\partial z}\hat{e}_z \tag{11}$$

The vector components of $\mathbf{E}_{\text{ring}}$ are

$$E_{\rho,\text{ring}} = \frac{q}{4\pi^2\epsilon_0}\frac{1}{\sqrt{\alpha\beta}\rho}\left[\beta K\left(\frac{4R\rho}{\alpha}\right) - \gamma \mathrm{E}\left(\frac{4R\rho}{\alpha}\right)\right] \tag{12}$$

$$E_{\theta,\text{ring}} = 0 \tag{13}$$

$$E_{z,\text{ring}} = \frac{q}{2\pi^2\epsilon_0}\frac{z}{\sqrt{\alpha\beta}}\mathrm{E}\left(\frac{4R\rho}{\alpha}\right) \tag{14}$$

In Eqs. (12) and (14), E is the complete elliptic integral of the second kind and

$$\beta = (R - \rho)^2 + z^2 \tag{15}$$

$$\gamma = R^2 - \rho^2 + z^2 \tag{16}$$

Taking the radius of the point **P** on the charged ring going to zero, $\rho \to 0$, recovers the form for the z component of the electric field magnitude along the z axis given by Brockhaus et al. [9],

$$E_{z,\text{ring}}(0, z) = \frac{1}{4\pi\epsilon_0}\frac{qz}{(R^2 + z^2)^{3/2}} \tag{17}$$

C. Cylindrical Plasma Adaptive Optics Lens Model

To model the PAO lens, two oppositely charged rings are superimposed as shown in Fig. 9. Both of the rings have a diameter D and they are separated by a gap distance d. The voltage potential and electric field components between the two rings are

$$V = V_{\text{ring}}(\rho, z - d/2) - V_{\text{ring}}(\rho, z + d/2) \tag{18}$$

$$E_\rho = E_{\rho,\text{ring}}(\rho, z - d/2) - E_{\rho,\text{ring}}(\rho, z + d/2) \tag{19}$$

$$E_\theta = 0 \tag{20}$$

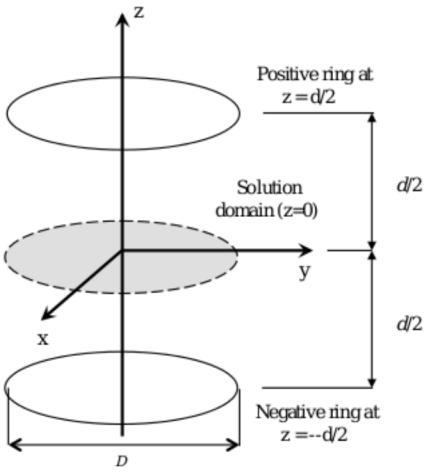

Fig. 9 Illustration of two charged rings superimposed and separated by a distance d.

$$E_z = E_{z,\text{ring}}(\rho, z - d/2) - E_{z,\text{ring}}(\rho, z + d/2) \tag{21}$$

The magnitude of the electric field is a spatial function of ρ and z, namely,

$$E(\rho, z) = \sqrt{E_\rho(\rho, z)^2 + E_z(\rho, z)^2} \tag{22}$$

In the experiments, the z plane was arbitrary. Therefore, the model result for the electric field magnitude that applies to the PAO lens experiments is

$$E(\rho) = \sqrt{E_\rho(\rho)^2 + E_z(\rho)^2} \tag{23}$$

VII. Theory Results

Solutions for the electric field magnitude inside the PAO lens were generated using Eq. (23). Variables were chosen to mimic the experimental setup. All the variables used in the solutions are listed in Table 2. The solutions for the 12 gap distances tested in the experiment are shown in Fig. 10. The gray level scales in Fig. 10 vary from image to image to better emphasize the respective electric field spatial structure.

The electric field profiles from the theoretical model appear to be very similar to the experimental light emission profiles. At $d/D = 0.3$, the concentration of highest electric field magnitude is thin and along the inside wall of the cylindrical PAO lens. As the gap distance, d, increases, the concentration of highest electric field magnitude thickens and pulls away from the inside walls. Above $d/D = 1.2$, the concentration of highest electric field magnitude coalesces into the center of the cylindrical lens.

VIII. Comparison Between Experiment and Theory

The experimental data gave average radial profiles of the plasma luminescence, which is a quantity related to the level of plasma ionization inside the PAO lens. The theoretical model gave radial profiles of electric field magnitude inside the PAO lens. It is generally

Table 2 Values used in the theoretical modeling

Parameter	Value(s)
r	$[0, R]$
z	0
d	{2.7, 3.6, 4.5, 5.4, 6.3, 7.2, 8.1, 9.0, 9.9, 10.8, 11.25, 12.6}
D	9.0
q	1

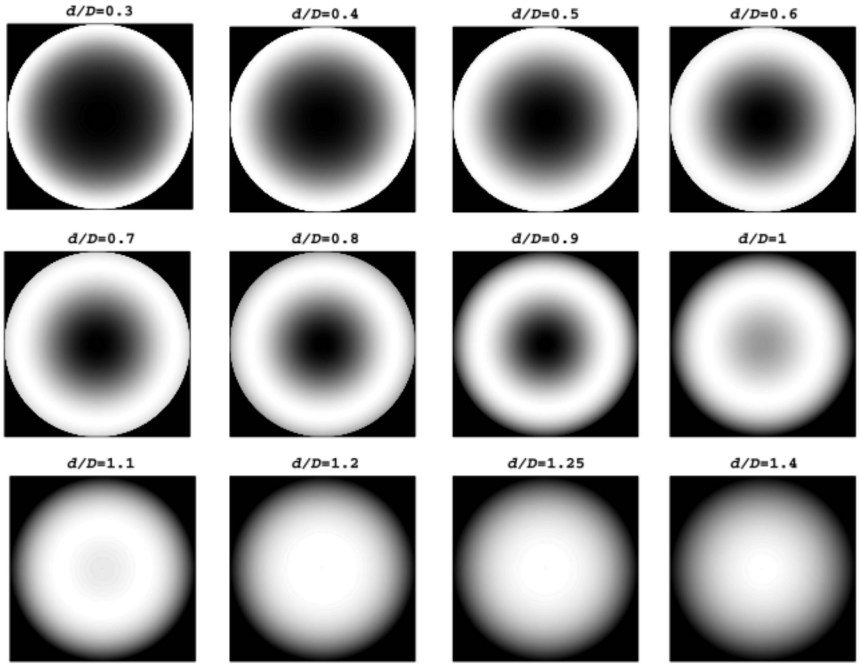

Fig. 10 Theoretical profiles of the electric field magnitude for different d/D ratios.

known that the degree of ionization, indicated by the plasma luminescence, correlates with the strength of the electric field. Therefore, it is valid to qualitatively compare the experimental luminescence profiles to the radial profiles of the electric field from the theoretical model.

Figure 11 shows plots of the radial profiles of the plasma luminescence for the different d/D values from the experiments. The comparable plots of the radial profiles of the electric field magnitude from the theoretical model are shown in Fig. 12. In both sets of plots, the center of the cylindrical PAO lens is at the plot origin, and the maximum inside radius is at the largest value on the abscissa. The dashed vertical line in each of the plots shows the radial location of the respective quantity maximum. The location of the quantity maximum is designated $\rho_{\max}$. The dashed-dotted vertical line shows the radial location of an inflection in the respective radial distributions.

The locations of the maximum plasma illumination as a function of d/D from the experiments is compared to the location of the maximum electric field magnitude in Fig. 13. In this case, the radial location is normalized by the inside radius of the cylindrical PAO and designated as

$$\rho^*_{\max} = \frac{\rho_{\max}}{R}$$

The symbols in the plot correspond to the experiment. The curve corresponds to the theory.

The experiment and theory show good agreement for $d/D \leq 0.5$, where the plasma forms very close to the inside wall of the cylindrical

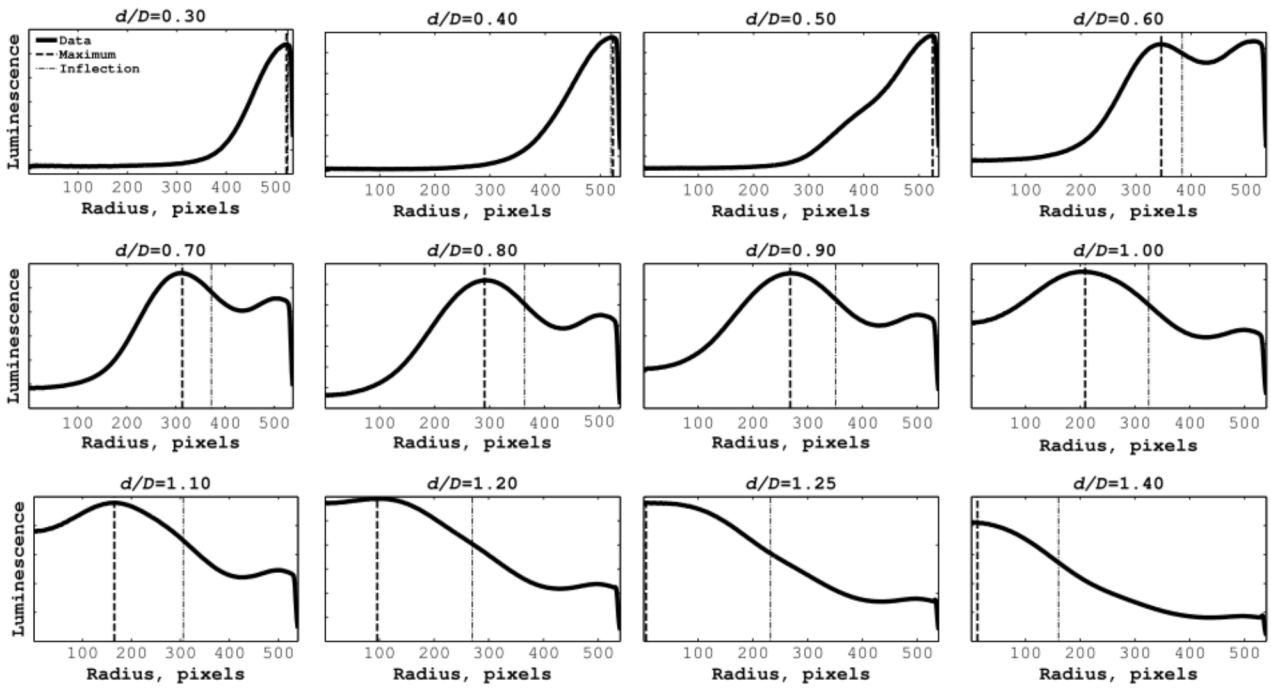

Fig. 11 Experimental radial profiles of plasma luminescence for different d/D ratios.

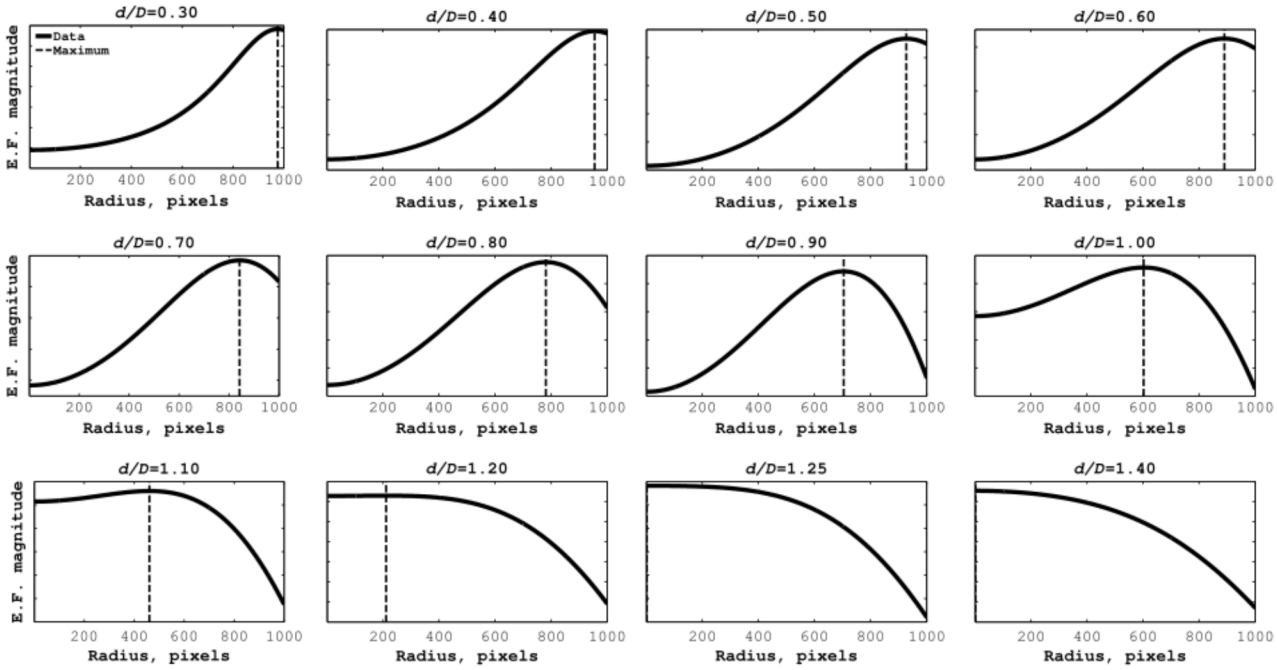

Fig. 12 Theoretical radial profiles of electric field magnitude for different d/D ratios.

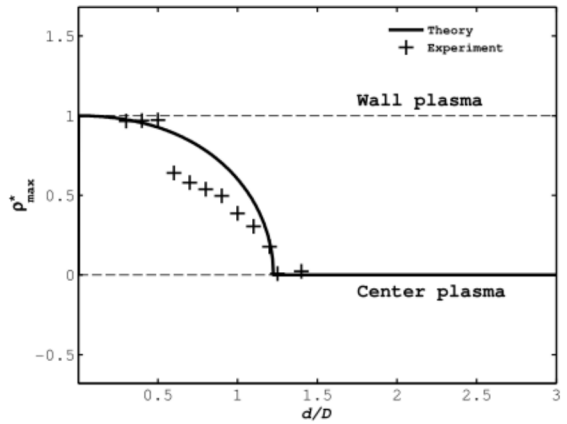

Fig. 13 Comparison of experimental and theoretical results normalized by the total radius.

PAO. The agreement is also very good for $d/D \geq 1.1$, where the plasma forms in the center of the cylindrical PAO. The good agreement at the larger d/D values confirms a "critical" value of $d/D = 1.22$ that is needed to concentrate the plasma in the center of the cylindrical PAO. This is the optimal configuration for the PAO operation.

We note that the agreement between the experiment and theory is not as good for $0.6 < d/D < 1.1$. In comparing the plots in Figs. 11 and 12, we note that the radial profiles from the experiments have inflection points that the theory does not predict. The radial locations of the inflection points were noted in the plots by the vertical dashed-dotted lines. The reason for the inflection points in the profiles has not been determined. One supposition is that it may be due to space charge accumulation on the inside surface of the borosilicate tube, which acts as a dielectric layer in the PAO design. If present, the theory does not account for this.

To better compare the experiment with the theory, a new normalization method for the experimental data was introduced. This used the radial location of the inflection point, $\rho_{\text{inflection}}$, instead of the cylinder radius, R, to normalize the radial location where the maximum occurred, namely,

$$\rho^{**}_{\max} = \frac{\rho_{\max}}{\rho_{\text{inflection}}} \tag{24}$$

The comparison between the experiment and theory using this new normalization is shown in Fig. 14. This new normalization significantly improved the agreement between the experiment and theory, especially for $0.6 < d/D < 1.1$. This would suggest that the location of the inflection in the illumination might represent a virtual surface inside of the physical cylindrical surface of the PAO. Further experiments will seek to quantify the reason for this.

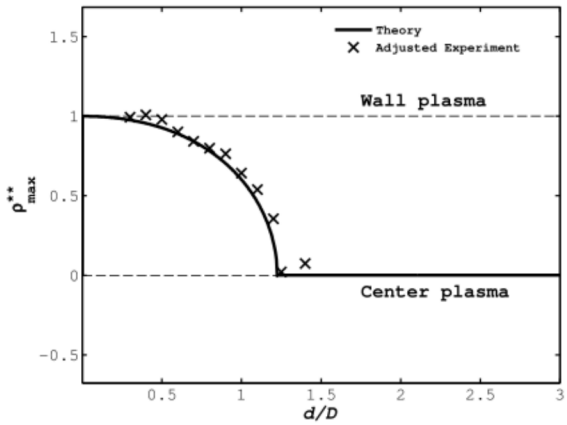

Fig. 14 Comparison of experimental and theoretical results normalized by the inflection radius.

IX. Conclusions

The cylindrical plasma adaptive optics (PAO) lens has promising features for use as an adaptive optics element. The work presented here has focused on optimizing the geometry of a cylindrical PAO lens by parameterizing the electrode-gap distance to diameter ratio, d/D. This was prompted by the observation that there appeared to be a critical value of d/D that determined if the plasma formed on the inside wall or in the center of the cylindrical lens, which was optimal for the optics application.

Experiments were performed in which the radial distribution of the plasma illumination was documented for different d/D values. The results were compared against a theoretical model for two charged rings. The agreement between the theory and experiment was excellent and confirmed a critical $d/D = 1.22$.

The comparison between experiment and theory highlighted physics that suggests that a virtual inside surface, which is possibly due to charge accumulation, may be present and not accounted for in the theoretical model. Future work will seek to quantify this issue. The theoretical model, however, has provided a necessary scaling relation that can be used to miniaturize the PAO elements for use in an adaptable array that can provide spatial wavefront corrections for aero-optics applications.

References

[1] Cicchiello, J. M., and and Jumper, E. J., "Far-Field Optical Degradation Due to Near-Field Transmission Through a Turbulent Heated Jet," *Applied Optics*, Vol. 36, No. 25, 1997, pp. 6441–6452. doi:10.1364/AO.36.006441

[2] Porter, C., Gordeyev, S., Zenk, M., and Jumper, E., "Flight Measurements of Aero-Optical Distortions from a Flatwindowed Turret on the Airborne Aero-Optics Laboratory (AAOL)," AIAA Paper 2011-3280, 2011.

[3] Becker, K., Kogelschatz, U., Schoenbach, K., and Barker, R., *Non-Equilibrium Air Plasmas at Atmosphericic Pressure*, Institute of Physics Publishing, Philadelphia, 2004, pp. 488–491.

[4] Uhm, H. S., Choi, E. H., and Jung, K. B., "Influence of Gas Pressure on 147 nm Emission Properties of Plasma Display Panel," *Japanese Journal of Applied Physics*, Vol. 44, No. 8, 2005, pp. L271–L274. doi:10.1143/JJAP.44.L271

[5] Neiswander, B., Matlis, E., and Corke, T., "Plasma Lens for Optical Path Difference Control," *AIAA Journal*, Vol. 50, No. 1, Jan. 2012, pp. 123–130. doi:10.2514/1.J051175

[6] Boeuf, J., "Plasma Display Panels: Physics, Recent Developments and Key Issues," *Journal of Physics D: Applied Physics*, Vol. 36, No. 6, 2003, p. R53. doi:10.1088/0022-3727/36/6/201

[7] Good, R., "Elliptic Integrals, the Forgotten Functions," *European Journal of Physics*, Vol. 22, No. 2, 2001, p. 119. doi:10.1088/0143-0807/22/2/303

[8] Byrd, P., and Friedman, M., *Handbook of Elliptic Integrals for Engineers and Scientists*, 2nd ed., Springer–Verlag, Berlin, 1971, p. 172.

[9] Brockhaus, A., Sauerbier, R., and Engemann, J., "Comparison of Three Excitation Schemes for Cylindrical Dielectric Barrier Discharges," *The European Physical Journal Applied Physics*, Vol. 47, No. 2, April 2009, p. 22809. doi:10.1051/epjap/2009083

L. Cattafesta
Associate Editor